Tundra greenness

Frost, G. V.; Macander, M. J. ; Bhatt, Uma S.; Epstein, Howard E.; Berner, Logan T. ; Bjerke, Jarle W. ; Forbes, Bruce C.; Goetz, Scott J; Lara, M. J.; Park, T; Phoenix, Gareth K.; Raynolds, Martha K; Tømmervik, Hans; Walker, Donald A.

Published in:
Bulletin of the American Meteorological Society

DOI:
10.1175/BAMS-D-21-0086.1

Published: 01.01.2021

Document Version
Publisher's PDF, also known as Version of record

Citation for pulished version (APA):
Frost, G. V., Macander, M. J., Bhatt, U. S., Epstein, H. E., Berner, L. T., Bjerke, J. W., Forbes, B. C., Goetz, S. J., Lara, M. J., Park, T., Phoenix, G. K., Raynolds, M. K., Tømmervik, H., & Walker, D. A. (2021). Tundra greenness. *Bulletin of the American Meteorological Society*, *101*(8, Special Supplement), S297–S303. https://doi.org/10.1175/BAMS-D-21-0086.1

STATE OF THE CLIMATE IN 2020

THE ARCTIC

M. L. Druckenmiller, T. Moon, and R. Thoman, Eds.

Special Online Supplement to the *Bulletin of the American Meteorological Society* Vol.102, No. 8, August, 2021

https://doi.org/10.1175/BAMS-D-21-0086.1

Corresponding author: Matthew L. Druckenmiller / druckenmiller@colorado.edu

Sites in Svalbard displayed similar ALT values to the two previous years, values that were approximately 0.13 m above the 2003–12 mean (Fig. 5.23). ALT for Greenland in 2020 was similar to that in 2019, 0.08 m above the 2003–12 mean (Strand et al. 2020).

Sites in West and East Siberia reported increased ALT in 2020, continuing the general trend, with the average ALT (1.46 m) for West Siberia being a new record maximum for the observation period (Fig. 5.23). Significant ALT reduction was reported in 2020 for sites in the Russian European North and Chukotka, but these values are based on fewer sites and may not be representative of regional trends previously reported (Abramov et al. 2019; Vasiliev et al. 2020).

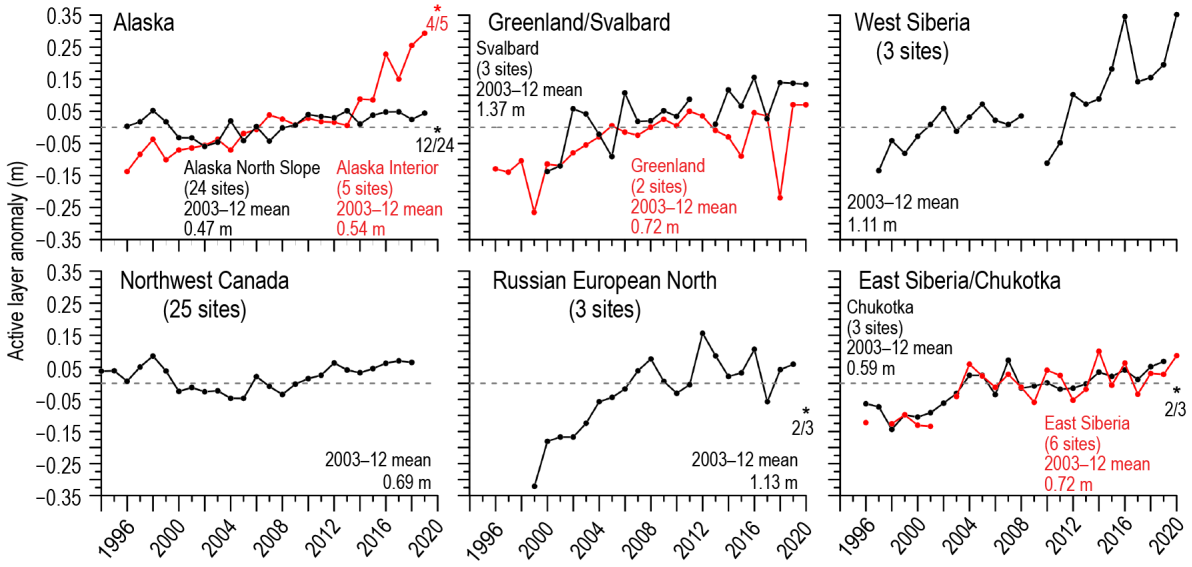

Fig. 5.23. Long-term active layer thickness anomalies in six different Arctic regions as observed by the Circumpolar Active Layer Monitoring (CALM) program. The data are shown as annual anomalies (m) relative to the mean value for the reference period 2003–12. Positive and negative anomaly values indicate the active layer is thicker or thinner than the 10-year mean values, respectively. The number of sites varies by region (numbers provided on figure), because only sites with >20 years of continuous thaw depth observations from the end of the thaw season were included. Asterisks on the figure represent 2020 data, as observations from fewer sites (number provided beside asterisks) were possible due to pandemic-related restrictions. Site-specific data are available at www2.gwu.edu/~calm/.

i. Tundra greenness—G. V. Frost, M. J. Macander, U. S. Bhatt, H. E. Epstein, L. T. Berner, J. W. Bjerke, B. C. Forbes, S. J. Goetz, M. J. Lara, T. Park, G. K. Phoenix, M. K. Raynolds, H. Tømmervik, and D. A. Walker

Occupying Earth's northernmost lands, the Arctic tundra biome is a focal point of global environmental change because vegetation and underlying permafrost soils are strongly influenced by warming air temperatures and interactions with sea ice loss in the adjacent Arctic Ocean (Lawrence et al. 2008; Bhatt et al. 2010; Serreze and Barry 2011; sections 5b–d). One of the most striking consequences of the Arctic's warming climate has been an increase in the productivity ("greenness") of tundra vegetation, which is largely governed by summer temperature (Berner et al. 2020; Bjorkman et al. 2020). Tundra greenness has been monitored by Earth-observing satellites since 1982 and a growing constellation of spaceborne sensors provide increasingly detailed observations of Arctic ecosystems.

The spaceborne record of global vegetation productivity began in late 1981 using the Advanced Very High Resolution Radiometer (AVHRR), a sensor that collects daily observations and continues to operate onboard polar-orbiting satellites today. The long-term dataset reported here is the Global Inventory Modeling and Mapping Studies 3g V1.2 dataset (GIMMS-3g+), which is based on corrected and calibrated AVHRR data with a spatial resolution of about 8 km (Pinzon and Tucker 2014). At the time of this writing, however, processed GIMMS-3g+ data are available only through the 2019 growing season. Therefore, we also report observations from the Moderate Resolution

Imaging Spectroradiometer (MODIS), a more modern sensor with a higher spatial resolution of 500 m that became operational in 2000. Both AVHRR and MODIS monitor vegetation productivity using the Normalized Difference Vegetation Index (NDVI), a spectral dimensionless metric of vegetation productivity that exploits the unique way in which green vegetation reflects light in the red and near-infrared wavelengths. Here we summarize the GIMMS-3g+ and MODIS records for Maximum NDVI (MaxNDVI), the peak yearly value that is strongly correlated with the biomass of aboveground vegetation during midsummer (Raynolds et al. 2012). For MODIS, we computed MaxNDVI from daily Nadir Bidirectional Reflectance Distribution Function Adjusted Reflectance data (MCD43A4, version 6; Schaaf 2020).

The GIMMS-3g+ and MODIS records both indicate that MaxNDVI has increased across most of the circumpolar Arctic during 1982–2019 and 2000–20, respectively (Figs. 5.24a,b). Although the two datasets consider different periods, several Arctic regions stand out as change "hotspots" in both records. In North America, greening has been strongest in northern Alaska and mainland Canada, while trends have been flat or negative ("browning") in parts of the Canadian Arctic Archipelago. In Eurasia, strong greening has occurred in the Russian Far East (Chukotka), but browning is evident in the East Siberian Sea sector and portions of the Taymyr Peninsula. Trends in northwestern Siberia and the European Arctic, however, are somewhat mixed for both time periods. Regional differences in Arctic greenness highlight that ecosystem responses to climate change are also influenced by the local properties of sea ice, permafrost, seasonal snow, soil composition and moisture, disturbance processes, wildlife, and human activities (Buchwal et al. 2020; Skarin et al. 2020; Epstein et al. 2021; Kemppinen et al. 2021; Kropp et al. 2021).

The MODIS MCD43A4 record complements the GIMMS-3g+ dataset for the 21-year period since 2000 and provides observations for the 2020 growing season. The mean circumpolar MaxNDVI value in 2020 was by far the highest in the MODIS record (3.4% higher than the previous high set in 2012). Circumpolar MaxNDVI increased 4.0% from the 2019 value; increases from the previous year were larger for the North American Arctic (5.6%) than for Eurasia (2.0%). The overall trend in circumpolar MaxNDVI remains strongly positive and circumpolar values have exceeded the 21-year mean in nine of the last 10 growing seasons (Fig. 5.25). The GIMMS-3g+ record also indicates increasing mean circumpolar MaxNDVI for both the full record (1982–2019) and the period of overlap with MODIS (2000–2019).

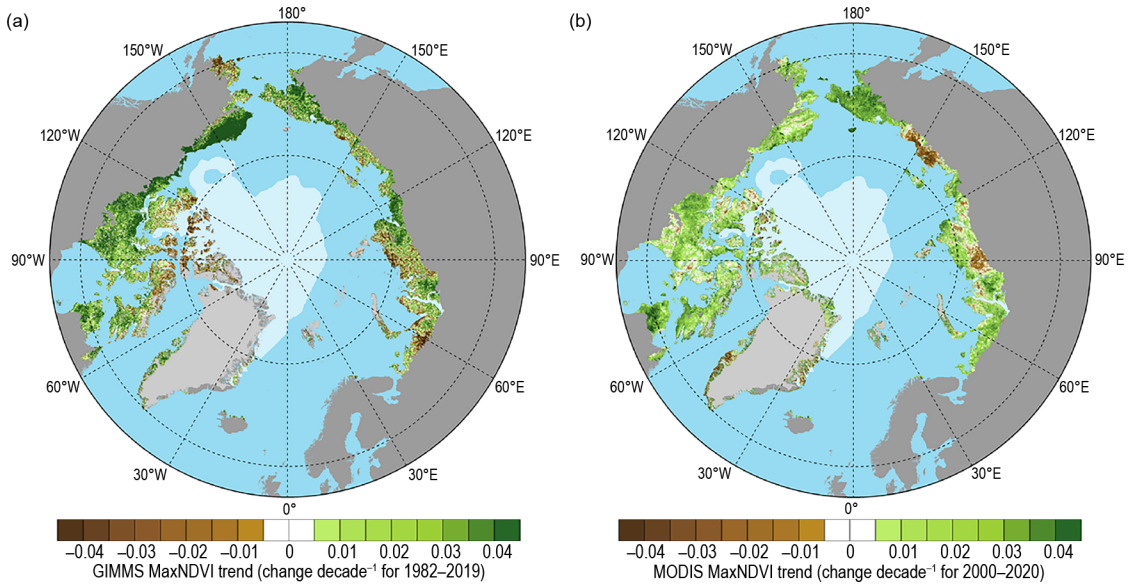

Fig. 5.24. Magnitude of the MaxNDVI trend calculated as the change decade^{-1} over a least squares, linear fit trend line for (a) 1982–2019 based on the GIMMS-3g+ dataset, and (b) 2000–20 based on the MODIS MCD43A4 dataset. GIMMS-3g+ data for 2020 were not available for this report due to data-processing requirements.

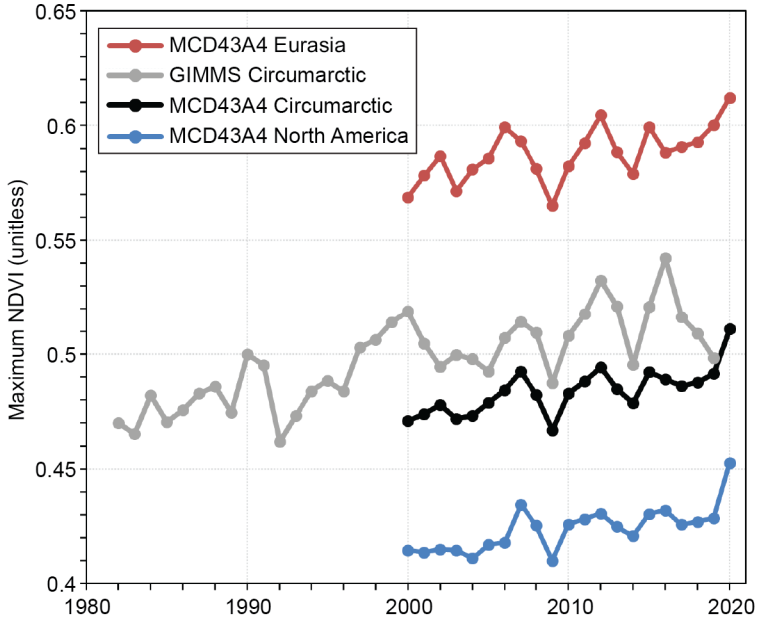

Fig. 5.25. Time series of MaxNDVI from the MODIS MCD43A4 (2000–20) dataset for the Eurasian Arctic (red), North American Arctic (blue), and the circumpolar Arctic (black), and from the long-term GIMMS-3g+ (1982–2019) dataset for the circumpolar Arctic (in gray).

Recent remote sensing- and field-based studies provide context for understanding changes in vegetation and ground conditions that correlate with MaxNDVI trends. Many site-specific studies have detected increased growth and expansion of tundra shrubs, such as birches (*Betula*), willows (*Salix*), and alders (*Alnus*; Andreu-Hayles et al. 2020; Liljedahl et al. 2020; Shevtsova et al. 2020). Spaceborne observations also indicate changes in growing season length and the timing of phenological events such as spring snowmelt (section 5f), vegetation green-up, and autumn senescence. For example, a recent analysis of vegetation phenology using MODIS NDVI data revealed that the 2020 Arctic growing season began and ended on average over 5 days earlier and 2 days later, respectively, relative to the 2000–10 baseline (section 2h4). The start of the 2020 growing season was particularly early in the Eurasian Arctic, where green-up occurred about 9 days earlier than average due to warm spring temperatures and early snowmelt. In Svalbard, Vickers et al. (2020) evaluated snow cover using MODIS data and concluded that the length of the growing season increased by 4.2 days decade^{-1} since 2000. Moreover, a study of MaxNDVI over central Svalbard from 1986 to 2015 linked local greening to increasing temperature; however, the pace of greening was slower during the second half of the study period, which may be attributed to more frequent extreme winter warming events that can damage vegetation (Vickers et al. 2016).

Die-back or removal of vegetation can also be caused by landscape disturbances, including wildfire (Heim et al. 2021; Sidebar 5.1) and permafrost thaw (Verdonen et al. 2020; Chen et al. 2021; Swanson 2021; section 5h), as well as herbivore and pest outbreaks (Lund et al. 2017; Prendin et al. 2020). Severe event-driven browning has led to major reductions in carbon dioxide uptake by tundra plants in the European Arctic (Treharne et al. 2020). While Arctic warming is likely to continue to drive greening, drivers of browning are also increasing in frequency (Landrum and Holland 2020; Myers-Smith et al. 2020; Wu et al. 2020), highlighting the emergence of increased variability as a component of Arctic climate change.

j. Ozone and ultraviolet radiation—G. H. Bernhard, V. E. Fioletov, J.-U. Grooß, I. Ialongo, B. Johnsen, K. Lakkala, G. L. Manney, R. Müller, and T. Svendby

Past emissions of man-made chlorine-containing substances have caused substantial chemical depletion of ozone in the stratosphere (WMO 2018). The resulting ozone loss led to increases of ultraviolet (UV) radiation at Earth's surface with adverse effects on human health and the

environment (EEAP 2019; Neale et al. 2021). The chemical destruction of polar ozone occurs within a cold stratospheric cyclone known as the polar vortex, which forms over the North Pole every year during winter (WMO 2018). The polar vortex between December 2019 and March 2020 was the strongest on record since the start of satellite observations in 1979/80 (Lawrence et al. 2020) and affected stratospheric ozone concentrations in the Northern Hemisphere (NH) until August 2020.

1) Ozone

Chemical processes that drive ozone depletion in the polar stratosphere are initiated at temperatures below about 195 K (–78°C) at altitudes of approximately 15 to 25 km. These low temperatures lead to the formation of polar stratospheric clouds (PSCs), which act as a catalyst to transform inactive forms of chlorine-containing substances into active, ozone-destroying chlorine species. Temperatures were low enough for PSC formation by mid-November 2019, earlier than in any previous year since the start of observations by the *Aura* Microwave Limb Sounder (MLS) in 2004 (Manney et al. 2020; DeLand et al. 2020). Temperatures in the lower stratosphere remained conducive to PSC existence until 25 March 2020, which is about 1 month longer than typical (Lawrence et al. 2020). The number of days with temperatures low enough for sustaining PSCs was the highest since at least 1980 (Lawrence et al. 2020).

Because of the exceptionally strong, cold, and persistent stratospheric polar vortex, the potential for chemical ozone depletion was the highest since at least 2004. The MLS measurements near 16 km (the approximate altitude where most ozone loss typically occurs) show chlorine activation starting in mid-November 2019 and ozone declining by December (Fig. 5.26). From February 2020 onward, ozone concentrations were the lowest in the MLS record and remained below past measurements (2004–19) until May, exceeding the ozone loss observed in the previous record years of 2010/11 and 2015/16.

The low ozone concentrations in the lower stratosphere during winter/spring 2019/20 led to exceptionally small Arctic total ozone columns (TOC; i.e., ozone amounts integrated from the surface to the top of the atmosphere) between January and July 2020. The TOCs in February, March, and April 2020 averaged over the polar cap (latitudes ≥63°N) were the lowest of the satellite record starting in 1979 (Lawrence et al. 2020), with near-record lows also for January, May,

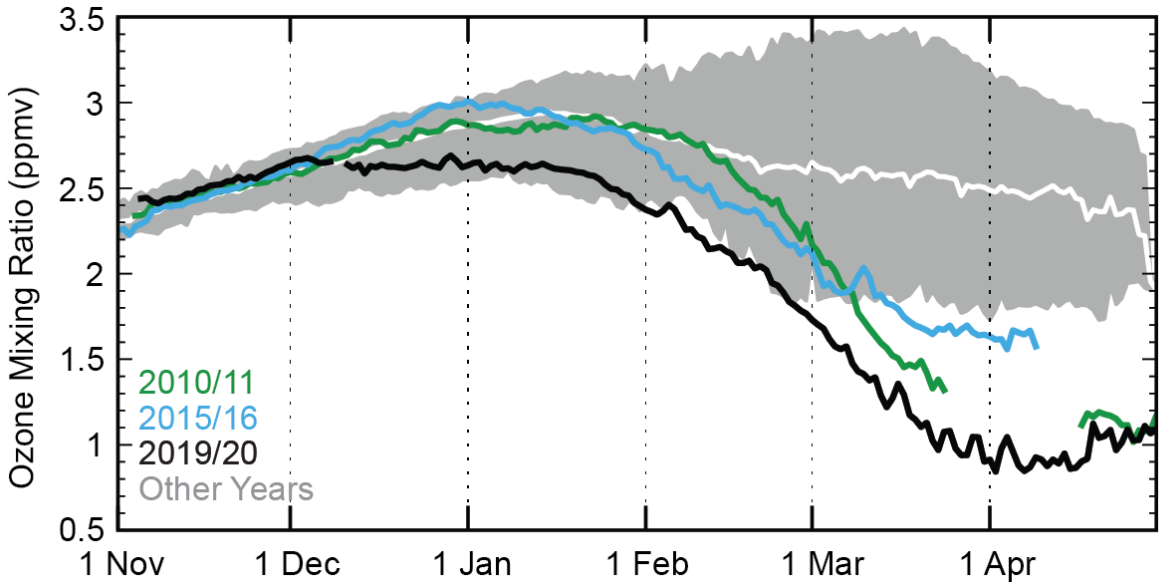

Fig. 5.26. Average ozone concentrations (expressed as ozone mixing ratio in ppmv) at an altitude of ~16 km for the area bounded by the polar vortex measured by *Aura* MLS. Data from 2019/20 (black), 2010/11 (green), and 2015/16 (cyan) are compared with the average (solid white) and minimum/maximum range (gray shading) from 2004/05 to 2018/19, excluding 2010/11 and 2015/16. The gap in the 2010/11 record is due to missing data; the 2015/16 record is foreshortened by the early vortex breakup that year (Manney and Lawrence 2016).

June, and July. While chemical ozone destruction ceased at the beginning of April 2020, TOCs over the NH remained depressed between May and August as ozone-depleted polar air mixed with air from midlatitudes.

Figure 5.27 focuses on the variation in TOC between 1979 and 2020 for March alone because March is the month with the largest potential for chemical ozone depletion in the Arctic (WMO 2018). Instead of illustrating the mean polar cap TOC discussed above, Fig. 5.27 shows the March minimum of the daily mean TOC within an area that encloses the polar vortex and is surrounded by the 63°N contour of "equivalent latitude" (Butchart and Remsberg 1986). In March 2020, the minimum Arctic daily TOC was 295 Dobson units (DU), which was the lowest value since the start of satellite observations in 1979 and 21% (79 DU) below the average of the observational record (374 DU).

Spatial deviations of monthly average TOCs from past (2005–19) averages (Fig. 5.28a) were estimated from Ozone Monitoring Instrument (OMI) measurements. In March 2020, TOC anomalies as large as –40% and exceeding 3 standard deviations were measured over northern Canada and the adjacent Arctic Ocean. In April, TOC anomalies up to –35% and exceeding 3 standard deviations were observed for virtually all areas north of 60°N. During the breakup of the polar vortex in May (Manney et al. 2020), areas with abnormally low (>3 std. dev.) TOCs still persisted over Siberia.

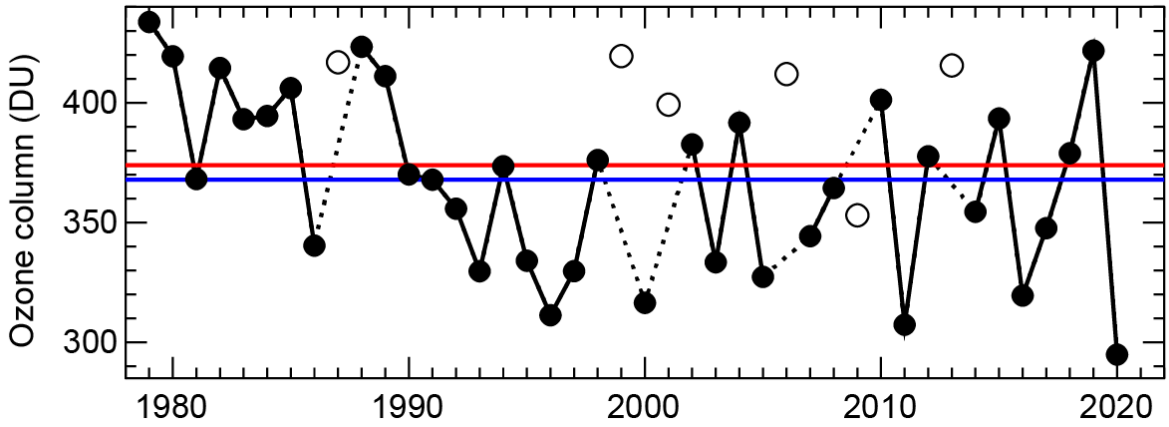

Fig. 5.27. Minimum of the daily average total ozone column (Dobson units, DU) for Mar poleward of 63°N equivalent latitude (Butchart and Remsberg 1986). Open circles represent years in which the polar vortex was not well-defined in Mar, resulting in relatively high values owing to mixing with lower latitude air masses and a lack of significant chemical ozone depletion. Red and blue lines indicate the average total ozone column for 1979–2019 and 2005–19, respectively. Ozone data for 1979–2016 are based on the combined total column ozone database version 3.4 produced by Bodeker Scientific (www.bodekerscientific.com/data/total-column-ozone). Ozone data for 2017–20 are from the OMI. The graph is adapted from Müller et al. (2008) and WMO (2018), updated using ERA5 reanalysis data (Hersbach et al. 2020) for determining equivalent latitude.

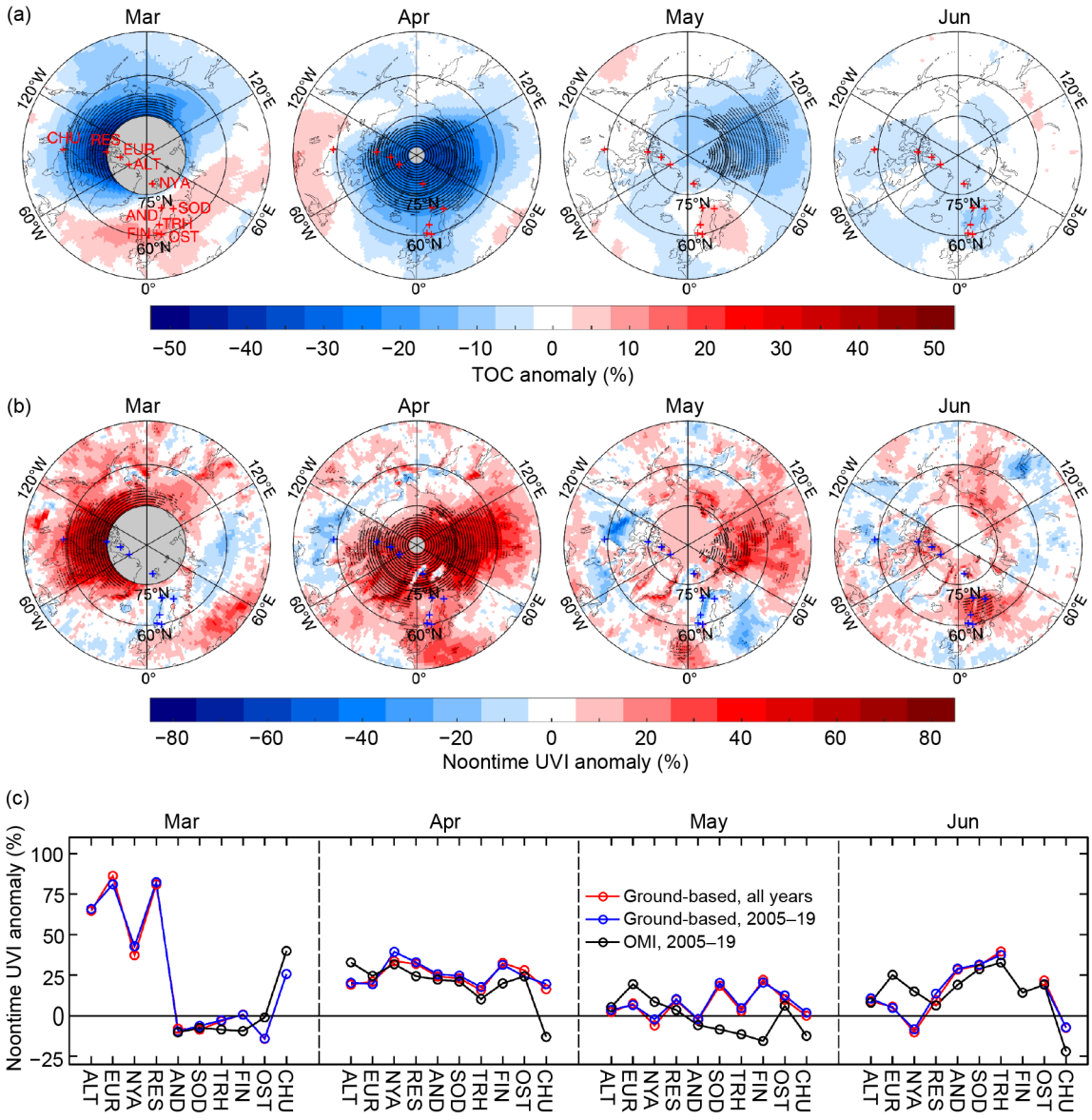

Fig. 5.28. Monthly mean anomaly maps of (a) total ozone column (%) and (b) noontime UV index (%) for Mar, Apr, May, and Jun 2020 relative to 2005–19 means. Stippling indicates pixels where anomalies exceed 3 std dev. Gray-shaded areas centered at the North Pole in the maps for Mar and Apr indicate latitudes where no Ozone Monitoring Instrument (OMI) data are available because of polar darkness. Locations of ground stations are indicated by crosses in every map, with labels added to the first map. Maps are based on the OMTO3 Level 3 total ozone product (Bhartia and Wellemeyer 2002). (c) Anomalies of monthly means of the noontime UV index (%) for 2020 derived from measurements at 10 ground stations (north to south along *x*-axis) relative to all years with available data (red) and 2005–19 (blue). The black datasets indicate anomalies for the same stations derived from OMI measurements (b) relative to 2005–19. Site acronyms are ALT: Alert (83°N); EUR: Eureka (80°N); NYA: Ny-Ålesund (79°N); RES: Resolute (75°N); AND: Andøya (69°N); SOD: Sodankylä (67°N); TRH: Trondheim (63°N); FIN: Finse (61°N); OST: Østerås (60°N); and CHU: Churchill (59°N). Figure adapted from Bernhard et al. (2020).

2) Ultraviolet radiation

UV radiation is quantified with the UV index (UVI), which measures the ability of UV radiation to cause erythema (sunburn) in human skin (WHO 2002). In addition to its dependence on TOC, the UVI depends on the sun angle, clouds, aerosols, and surface albedo (Weatherhead et al. 2005). In the Arctic, the UVI scale ranges from 0 to about 7; UVI values north of 80°N remain below 3.

On several days in 2020, UVIs observed by ground-based radiometers at 10 sites distributed across northern Canada and Europe exceeded historical (2005–19) means by more than 75% (Bernhard et al. 2020). At the Canadian sites, these means were surpassed by more than 6 standard deviations. Monthly mean UVIs were 75% higher than normal in northern Canada in March

2020 and elevated by about 25% at all sites in April 2020 (Bernhard et al. 2020). These large relative anomalies occurred early in the year when the Sun is still low in the sky. Therefore, UVI increases remained small in absolute terms and did not exceed typical summertime UVI values under clear skies.

Figure 5.28b quantifies spatial differences in monthly average noontime UVIs from past (2005–19) averages based on measurements by OMI. Areas with high UVIs roughly match areas with low TOCs (Fig. 5.28a), but UVI anomalies have larger spatial variability because of their added dependence on clouds. In March 2020, monthly average UVI anomalies over the Canadian Arctic and the adjacent Arctic Ocean ranged between 30% and 70%, often exceeding 3 standard deviations. In April 2020, UVI anomalies were positive over a vast area, including northern Canada, Greenland, northern Europe, and Siberia. The maximum anomaly was 78% and anomalies exceeded 3 standard deviations almost everywhere north of 70°N. In May 2020, UVI anomalies of up to 60% and exceeding 3 standard deviations were measured over Siberia. The UVIs in June were elevated by up to 30% over parts of Norway, Sweden, and Finland, resulting from a combination of negative TOC anomalies (Fig. 5.28a) and unusually fair weather with several cloudless days (Bernhard et al. 2020). Ground-based measurements generally confirm UVI anomalies derived from satellite data (Fig. 5.28c).